Assignment of the Raman Spectrum of Benzylic Amide [2]Catenane: Raman Microscopy Experiments and First-Principles Calculations

Carlos Romero-Muñiz,[*,†,§] Denís Paredes-Roibás,[‡,§] Concepción López,[¶] Antonio Hernanz,[‡] and José María Gavira-Vallejo[‡]

†*Departamento de Física Teórica de la Materia Condensada, Universidad Autónoma de Madrid, E-28049 Madrid, Spain*

‡*Departamento de Ciencias y Técnicas Fisicoquímicas, Facultad de Ciencias, Universidad Nacional de Educación a Distancia (UNED), Paseo de la Senda del Rey 9, E-28040 Madrid, Spain*

¶*Departamento de Química Orgánica y Bio-Orgánica, Facultad de Ciencias, Universidad Nacional de Educación a Distancia (UNED), Paseo de la Senda del Rey 9, E-28040 Madrid, Spain*

§*Contributed equally to this work*

E-mail: carlos.romero@uam.es

July 17, 2018

Abstract

In this work we use Raman spectroscopy and quantum first-principles calculations to unveil the experimental spectrum of a complex molecular solid like benzylic amide [2]catenane, a representative example of a mechanically interlocked molecular architecture. We use large-scale Density Functional Theory calculations to obtain the complete set of vibrational normal modes of the catenane crystal, whose unit cell contains 544 atoms. Subsequently, we demonstrate that these calculations are able to accurately reproduce the experimental Raman spectrum of this molecular compound, without introducing any empirical corrections or fittings in the calculated eigenfrequencies. Thanks to the good agreement between the experimental and theoretical spectra it is possible to carry out the complete assignment of the main vibrational modes responsible for the whole spectrum. A detailed description in terms of the usual internal coordinates is given for all these representative modes. This description, rather difficult from the experimental point of view, provides valuable information about the molecular structure of this compound, compatible with experimental evidences reported in the literature.

Abbreviations

DFT, MNR

1 Introduction

The main mechanically interlocked molecular architectures were known from the middle of the 20th century.[1] They are compounds, whose molecular subunits are linked mechanically as a consequence of their topology, instead of traditional chemical bonds. However, it was not until the early 90's when the pioneering work by B. L. Feringa, J. P. Sauvage, and J. F. Stoddart gave rise to the so-called template directed syntheses based on the preorganization of the reactants through non-covalent interactions. Thanks to this breakthrough, a precise control in the final cyclization reactions of the macrocyclic precursors was achieved, leading to the efficient production of hundreds of mechanically interlocked compounds like catenanes, rotaxanes and molecular knots.[2,3]

Compounds owning mechanical bonds display peculiar chemical properties distinctive from those of typical covalent materials. In particular, the incorporation of moieties with molecular recognition motifs opens the door to the possibility of building and designing artificial molecular machines at atomic level.[4,5] For this reason, this class of materials is of extreme importance and, at the same time, represents a challenge from the characterization point of view (both theoretical and experimental). This is due to their complex structure and the internal freedom of their building blocks, which includes the ability of the rings to rotate with respect to one another and other low-energy dynamic processes. This motion can be detected and measured by magnetic nuclear resonance spectroscopy.[6,7]

In this work, we focus on the benzylic amide [2]catenane, a representative example of a large family of molecules, first synthesized in 1995 through a self-assembly procedure.[8,9] It is one of the simplest [2]catenanes, constituted by two identical macrocycles that are mechanically interlocked. Each of them, in turn, are formed by four bound aromatic units (–C_6H_4–CO–NH-CH_2–) or (–C_6H_4–CH_2–NH-CO–), linked in *meta* or *para* positions, as depicted in Fig. 1. This compound has been extensively characterized by a number of different experimental techniques, including X-ray diffraction,[8] magnetic nuclear resonance spectroscopy,[6,9,10] X-ray photoelectron spectroscopy,[11] electron energy loss spectroscopy,[12]

vibrational spectroscopy[13,14] or inelastic neutron scattering.[15] In addition, the internal dynamics of this catenante has been also investigated with classical molecular dynamics,[6,13,16,17] paying special attention to the rotation of the rings. These studies reveal that the benzylic amide [2]catenane is very sensitive to its chemical environment as a consequence of the presence of strong polar groups C=O and N–H capable of interact with different external species via hydrogen bonds.[10,14]

In this work, we aim to study the vibrational spectrum of this catenane using a combination of Raman microscopy experiments and quantum first-principles calculation. Unlike in earlier studies,[13,14,16] in which the quantum description of such a large and complex molecular solid was unaffordable from the computational point of view, we use calculations based on Density Functional Theory to determine both the vibrational modes of the catenane crystal and their Raman intensity. So far, this kind of analysis at quantum level had been restricted to those systems with smaller unit cells, mainly inorganic compounds.[18–22] However, in the present work, we disclose the Raman spectrum of such a complex molecular solid, finding a very good agreement between the theoretical calculations and the experimental results. This fair agreement allows us to perform a complete assignment of all the peaks appearing in the experimental Raman spectrum, providing the corresponding geometric description of the relevant modes. Therefore, the interest of this work is twofold. On the one hand, our study devises a simple procedure to accurately determine the vibrational spectrum of large systems containing hundreds of atoms in the unit cell. Besides, it is general method, applicable either for molecules or crystalline solids. On the other hand, it represents a significant progress in Raman spectroscopy, where often the extraction of molecular-scale features of complex material by spectra analysis might be rather difficult. Since most of the relevant Raman active modes have been properly assigned, these results will shed new light in further studies involving related molecular systems.

2 Experiments

2.1 Synthesis

The synthesis of the benzylic amide [2]catenane (i.e. IUPAC name [2] (1,7,14,20-Tetraaza-2,6,15,19-tetraoxo-3,5,9,12,16,18,22,25-tetrabenzocyclohexacosane)-(1',7',14',20'-tetraaza-2',6',-15',19'-tetraoxo-3',5',9',12',16',18',22',25'-tetrabenzocyclohexacosane) catenane) was carried out following the method described in ref. 13. 0.921 g (14.627 mmol) of triethylamine were dissolved in 100 mL of anhydrous chloroform, and it was stirred for half an hour in an argon atmosphere in a three-neck angled round bottom flask. Then, 0.665 g (3.286 mmol) of *p*-xylylene diamine and 0.447 g (3.313 mmol) of isophthaloyl chloride were dissolved in two flasks containing 100 mL of anhydrous chloroform each one. These solutions were transferred into two isobaric funnels and both were attached to the three-neck round flask. The solutions were mixed simultaneously for half an hour. The resulting solution was kept in agitation for 24 hours. Later, the solution was washed with 3×100 mL of HCl (1M) and 3×100 mL of NaOH (1M). The organic layer was dried with magnesium sulfate and the solvent in this layer was evaporated in a rotary evaporator. Around one half of the final product was recrystallized in order to obtain crystals large enough to facilitate their study by micro-Raman (μ-Raman). For this purpose, we dissolved the product in methanol and acetone and left it in a crystallizer for a week.

To confirm that we got the desired catenane, solution Nuclear Magnetic Resonance (NMR) spectra were recorded on a Bruker DRX 400 (9.4 Tesla, 400.13 MHz for ^{1}H and 100.62 MHz for ^{13}C) using a 5 mm QNP direct-detection probehead equipped with a z-gradient coil, at 300 K. Chemical shifts (δ in ppm) are given from internal solvent, DMSO-d_6 2.49 for ^{1}H and 39.5 for ^{13}C. We got for ^{1}H NMR δ = 8.47 (8H, s), 7.95 (4H, d), 7.80 (8H, d), 7.41 (4H, t), 6.65 (16H, s) and 3.92 (16H, s). For ^{13}C NMR, we got δ = 165.8, 137.2, 134.2, 129.6, 128.2, 126.6 and 42.8. These results are consistent with those of previous works.[8,9]

2.2 Raman spectroscopy

The equipment used was a Jobin Yvon spectrophotometer model LabRam-IR HR-800 with a focal length of 800 mm, a grating of 1800 grooves mm, confocal pinhole set at 100 μm and a Peltier refrigerated CCD (1024 $\times$ 256 pixels). These conditions and excitation with the 632.8 nm line of a He/Ne laser give rise to an average spectral resolution of 1 cm^{-1} in the wavenumber range of $100 - 1700$ cm^{-1}. The sine bar linearity of the spectrograph was adjusted using the fluorescent lamps of the lab (zero-order position) and the lines at 640.22 and 837.76 nm of a Ne lamp. The spectrophotometer was coupled to an Olympus BX41 confocal optical microscope. The confocality of the instrument was refined using the 519.97 cm^{-1} line of a silicon wafer. The laser effective power at the sample position using 50$\times$ and 100$\times$ objectives was kept at 250 and 225 μW respectively in order to avoid sample alteration. The indicated conditions result in a lateral resolving power of $\sim 1 - 2$ μm (100$\times$ objective lens) and $\sim$ 5 μm (50$\times$ objective lens) at the specimen. Wavenumber shift calibration[23] with 4-acetamidophenol, naphthalene and sulfur in the $150 - 3100$ cm^{-1} range using the same recording conditions resulted in a mean deviation of $\Delta\nu_{\text{cal}} - \Delta\nu_{\text{obs}} = 0.96 \pm 0.75$ cm^{-1} (t_{Student} of 95%). The spectral integration time was 20 s, and 20 records were accumulated in order to achieve spectra with an acceptable signal-to-noise ratio.

Depolarized Raman spectra of a large series of micro-crystals of the synthesized catenane have been collected. Raleigh line filter decay at low Stokes wavenumber has been baseline corrected using the *Multi-Point* algorithm (option "Level + Zero") of the Grams/AI$^{\text{TM}}$ v. 7.00 software, choosing around 10 points in each spectrum. No other numerical treatment or correction (smoothing, shifting, deconvolution, etc.) has been applied to the spectra.

3 First-principles calculations

In this work we have characterized the benzylic amide [2]catenane crystal by means of Density Functional Theory (DFT) calculations using the VASP (*Vienna Ab Initio Simulation*

Package) code.[24] A plane-wave basis sets with a cutoff of 400 eV was used together with PAW pseudopotentials[25,26] for all involved species (C, N, O and H). The PBE (Perdew-Burke-Ernzerhof) functional[27] was employed to reproduce the electronic exchange and correlation interactions supplemented with the semi-empricial D3 correction by S. Grimme,[28] to account for possible dispersion interactions.

A good equilibrium geometry for the catenane crystal was obtained combining electronic self-consistent loops (cutoff 10^{-6} eV) with a conjugate gradient optimization of the structure, until forces upon atoms were less than 0.005 eV/Å. This strict criterion is imposed to ensure the success of the subsequent normal mode analysis. During the ionic relaxation the lattice constants were kept fixed in order to preserve the original symmetry of the crystal structure and the reciprocal space was sampled with a $2 \times 2 \times 2$ Monkhorst-Pack grid,[29] due to the large size of the unit cell. The starting geometry was obtained from X-ray crystallographic data[8,30] (see Fig. 1c). This is an orthorhombic unit cell (a = 17.4382 Å, b = 12.4628 Å, c = 23.6926 Å, space group *Pbcn*), which contains four catenane molecules, leading to $136 \times 4 = 544$ total atoms per unit cell. Periodic boundary conditions are used to properly reproduce the crystal structure of the solid-state catenane.

The normal mode analysis was carried out by direct diagonalization of the Hessian matrix according to the classical analysis.[31,32] Under the harmonic approximation, the vibrational eigenmodes of a system constituted by N atoms are obtained after solving the corresponding eigenvalue problem given by

$$\sum_{j=1}^{3N}(f_{jk} - \lambda_{(n)}\delta_{jk})A_{j,(n)} = 0, \tag{1}$$

where f_{jk} is the mass-weighted Hessian matrix, $\lambda_{(n)} = (2\pi\nu_n)^2$ are the eigenvalues, related to the frequencies ν_n of the nth mode, and $A_{j,(n)}$ the elements of the corresponding eigenvectors. The Hessian matrix is numerically obtained through finite differences by computing the second derivatives of the energy with respect to the atomic positions. Six different

displacements (± 0.02 Å) per atom along the three Cartesian components are used in this algorithm. Notice that only those atoms belonging to the unit cell are considered in this calculation, giving rise to a total of $544 \times 3 - 6 = 1626$ normal modes. This procedure to calculate vibrational normal modes was tested with the benzamide molecule, closely related to structural building blocks of the catenane. A fair agreement with previous calculations and experimental Raman and infrared spectra[33] was found. See Table S1 in Supporting Information for further details.

The estimation of Raman intensities was carried out according to the scheme suggested by D. Porezag and M. R. Pederson.[34] In this approach, the scattered intensity I_n by the nth mode can be computed in terms of the variation of some elements (α_{ij}) of the polarizability tensor along that vibrational mode. In order to mimic our experimental conditions, we have to use this equation:[35]

$$I_n \propto \frac{1}{45}\left[45\left(\frac{d\alpha}{dQ}\right)^2_{eq} + 7\left(\frac{d\beta}{dQ}\right)^2_{eq}\right], \tag{2}$$

where α y β are two invariants of the polarizability tensor given by:

$$\alpha = \frac{1}{3}(\alpha_{11} + \alpha_{22} + \alpha_{33}), \tag{3}$$

$$\beta^2 = \frac{1}{2}[(\alpha_{11} - \alpha_{22})^2 + (\alpha_{11} - \alpha_{33})^2 + (\alpha_{22} - \alpha_{33})^2 + 6(\alpha_{12}^2 + \alpha_{13}^2 + \alpha_{23}^2)]. \tag{4}$$

The above expression is chosen because it is compatible with our experimental setup of Raman microscopy, in which non-polarized light is used as excitation source and the backscattered radiation (180°) is detected, leading to a depolarization ratio equals to one. Therefore, two additional calculations per mode must be carried out in order to determine the Raman intensity of each vibrational mode. Due to the large size of the system these calculations are restricted solely to the Γ point in the reciprocal space. In these calculations the polarizability tensor is calculated[36,37] in two different geometries slightly displaced along the corresponding normal model with respect the equilibrium position. In this way, the derivatives of Eq. (2) can be evaluated to obtain the Raman intensity. Finally, a discrete collection of scattered

intensities associated with each normal mode is obtained and the complete spectrum can be constructed by fitting each eigenfrequency to Lorentzian distributions according to:

$$F_n(\nu; I_n, \nu_n, \gamma) = \frac{I_n}{\pi} \frac{\gamma}{(\nu - \nu_n)^2 + \gamma^2}, \tag{5}$$

where γ was set to 10^{-3} cm^{-1} in order to achieve a good resolution.

4 Results and discussion

Following the synthetic procedure introduced in Sec. 2 we obtained several samples after the recrystallization process. The obtained crystals display a grain size distribution between 10 μm and 30 μm. They present a number of different morphologies due to their different spatial orientations and also to the appearance of different crystalline defects, like crystal twinning. In order to achieve the highest reliability degree in the experimental measurements many different crystals were analyzed by μ-Raman, including the most representative shapes found in the samples. In Fig. 2 we have selected four of them. S1 correspond to the amorphous catenane without further recrystallization, S2 has a rectangular shape, S3 a rhombic one and S4 is rectangular shaped. Since Raman microscopy allows us to analyze each individual crystal by focusing the laser beam appropriately, the exact measured points are indicated in each case with a red cross in Fig. 2.

As a result, four different Raman spectra were selected fulfilling the higuest quality criteria (i.e. high peak resolution, good signal/noise ratio, large enough intensities, etc.). They are shown (blue lines) in the left panel of Fig. 2. and are labeled as S1-S4, according to each microphotography. None of the spectra has been refined except for the removing of the Rayleigh contribution by subtracting the baselines. All these spectra were carefully analyzed in order to assign the proper location of all observed peaks, revealing that all of them are rather similar and essentially display the same features, in good agreement with previous results reported in the literature.[13] Notice that, slight differences in the intensity of

some peaks are found due to the different relative orientations of each crystal with respect to the incident radiation of the laser beam, and also the crystallinity degree. To overcome this issue, an averaged spectrum (red line) was obtained and it will be selected for further comparisons with the theoretical calculations. As expected this averaged spectrum resembles very much to S1, obtained from the amorphous sample without recrystalization. This fact reveals that the Raman fingerprint of this compound is essentially related to their molecular features and not to the long-range symmetry.

Theoretical calculations were carried out according to the approach detailed in Sec. 3. Fig. 3 shows the comparison between the theoretical Raman spectrum obtained with DFT calculations (black line) and the experimental spectrum (red line), the averaged one. We have chosen the averaged spectrum because in the theoretical calculation is assumed a random distribution of the sample dipoles with respect to the incident electromagnetic field, which is not the case in our μ-Raman experiments of single crystals. As already mentioned, this circumstance can be compensated by averaging over different spectra. Even so, we cannot expect, in this respect, a perfect agreement throughout the whole spectrum as a consequence of the intrinsic limitations of Eq. (2), used to calculate the Raman intensity. We cannot forget that this expression is the result of a relatively simple approximation based on a first-order approach. Therefore, we find a clear overestimation of the intensities in the high wavenumber shift region (> 2900 cm^{-1}). Conversely, this is not the case in the low wavenumber shift region where some intensity differences are expected due to the remaining Rayleight contribution to the total intensity in the experimental spectrum, which is completely absent in the calculations. However, the agreement between both spectra is remarkable regarding the matching of the peaks locations. Especially, taking into account that no rescaling fittings have been applied to the obtained eiegenfrequencies. This result reveals a high accuracy in the determination of the vibrational normal modes of the catenane crystal. Furthermore, we will see that the discrepancies found in the intensities can be drastically reduced if different regions of the spectrum, belonging to different kinds of

normal modes, are considered separately.

Once we have checked the good agreement between calculations and experiments we are in a position to assign the different vibrational modes corresponding to the experimental peaks of the spectrum. This theoretical assignment adds valuable information about the molecular structure of the compound, providing a geometrical description of those vibrational modes responsible for the experimentally observed peaks in the spectra. However, for such a complex case like the benzylic amide [2]catenane, this is not an easy task, due to the large number of degrees of freedom. In particular, 544 atoms per unit cell lead to a total of 1626 normal modes, although only a fraction of them will really contribute with a significant activity to the Raman spectrum. In order to select these more active modes we proceed by imposing some cutoffs for the intensity displayed by a given mode. In this way, only those modes with an intensity larger than the chosen cutoff (expressed with respect to the most intense mode) were selected for further analysis. Two different optimized values of cutoff were selected throughout the spectrum fulfilling two opposed requirements: they have to be low enough to minimize the number of active modes but, at the same time, large enough to keep the shape of the peaks displayed in the whole spectrum. With these criteria we retained 34 modes in the medium wavenumber shift region (between 600 cm^{-1} and 1700 cm^{-1}) and 23 modes in the high wavenumber shift part (> 2900 cm^{-1}), using the $\sim 25\%$ and the $\sim 50\%$ of the maximum intensity as cutoff values, respectively. Thank to this procedure, it is possible to carry out the complete assignment of the main vibrational modes responsible for the whole spectrum and the subsequent comparison with the experimental results. This is what is made in Table 1, where the complete mode list, together with a brief geometrical description of each one in terms of usual internal coordinates, is given with the associated peaks in both the theoretical and the experimental spectra. Notice that the assignment in the low wavenumber shift region (< 600 cm^{-1}) is much more complex and it has not been included in Table 1.

The comprehensive assignment collected in Table 1 discloses the Raman fingerprint of

this compound in terms of different kinds of vibrations of the catenane crystal. Before a deeper analysis, it is worth noting that a single peak in the experimental spectrum might be a complex overlap of several modes, and thus, its location may not exactly coincide with any normal mode. In addition, due to the crystal symmetry, there is a number of degenerate modes, which are equivalent and localized in different but equivalent groups of the unit cell (i.e. aromatic rings, carbonyl groups, etc.). In any case, it has been possible to assign every peak of the experimental spectrum to one or several discrete modes of the theoretical calculation. To get further insight of the spectrum we have divided the wavenumber shift range in four different regions associated with characteristic vibrations: (i) $[0, 600]$ cm^{-1}, (ii) $[600, 1100]$ cm^{-1}, (iii) $[1100, 1700]$ cm^{-1} and (iv) $[2900, 3500]$ cm^{-1}. As usual, the empty region between 1700 cm^{-1} and 2900 cm^{-1} has been discarded for further analysis since it lacks of any relevant Raman fingerprint as shown in Figs. 2 and 3. In Fig 4 we show the decomposed Raman spectrum in these four regions compared with the theoretical calculation. Notice that in each region both spectra have been renormalized using the strongest line of each region, leading to a remarkable overall agreement also in the relative intensities. A different version of Fig. 4 can be found in the Supporting Information (Fig. S1), including the discrete set of calculated eigenvalues.

The region (i) corresponds to the very low energy range, typically associated with phonon modes and complex molecular vibrations based on collective oscillations involving most of the atoms in the unit cell. For this reason, a more detailed analysis of these complex modes in terms of normal coordinates is absent. This conclusion is supported by the inspection of the discrete set of normal models associated with the broad peaks observed in this region of the spectrum (see Supporting Information). Besides, it is well-known that for low energy modes the relaxation times involved in vibrational processes play a crucial role in the construction of the spectrum, leading to a significant variability in widths of the peaks. Thus, a direct comparison at quantitative level between theory and experiment becomes too difficult. However, Fig. 4a shows a good matching between μ-Raman and calculated spectra

at qualitative level.

In the region (ii) a peak-by-peak comparison is indeed possible (see Fig. 4b). According to our normal modes analysis this region is governed by skeletal modes preferentially involving the aromatic rings but also the bridging aliphatic chains. These modes include slight planar and non-planar ring deformations and especially strong centrosymmetric in-plane vibrations, resembling the typical benzene breathing mode. Notice how the most intense peak in this region correspond to these latter modes at $\sim$ 1000 cm^{-1} in combination with the lowest energetic stretching modes in the benzene rings.

The region (iii), which includes the wavenumber shifts between 1100 cm^{-1} and 1700 cm^{-1}, is the region which contains the largest amount of information in Raman spectroscopy, and therefore involves the largest number of Raman active modes. As it is observed in Table 1, there are still present some modes associated to the rings, mainly antisymmetric in-plane distortions, leading to a strong band in the spectrum around 1300 cm^{-1}, in combination with in plane CCN vibrations. However, in this region we have other typical vibration modes like torsion or CH_2 wagging, responsible for one strong peak at $\sim$1350 cm^{-1}. For higher wavenumber shifts in this region, benzene rings vibrations become progressively less prominent in favour of more energetic stretching modes of CN and CO, located at $\sim$ 1530 cm^{-1} and $\sim$ 1600 cm^{-1}, respectively (see Fig. 4c). This fact is in good agreement with previous experimental evidences in which it is demonstrated a systematic shift of these bands depending on the presence of different cations.[13,14] Since they come from strong polar bonds, it is expected a high interaction with ions via hydrogen bonds. Therefore, a high chemical sensitivity to the environment is displayed.

Lastly, the region (iv) correspond to the most energetic vibrations $>$ 2900 cm^{-1}. Note in Fig. 4d that here a slight discrepancy between calculated eigenfrequencies and experimental peaks is found. As it can be seen, the shape of both renormalized spectra is the same but a displacement between 50 and 80 cm^{-1} is found between both sets of peaks in Fig. 4d. However, in this high-energy region of the spectrum, such differences in Raman shifts represent

in the worse cases less than a 3% of uncertainty in the determination of the eigenfrequencies. Thus, we can still consider an accuracy level sufficient to proceed with the assignment. This region is essentially characterized by two different kinds of stretching vibrations: a strong stretching of CC in the aromatic rings located at $[2900 - 3000]$ cm^{-1} and the stretching of NH bonds located at $[3300 - 3400]$ cm^{-1}.

In summary, in this work we have carried out the assignment of the observed Raman bands of benzylic amide [2]catenane, which establishes a fundamental and useful basis for future studies on interactions, reactions and structural alterations of this compound by vibrational spectroscopy. Furthermore, this band assignment based on the geometrical description of most relevant normal modes involved, could very very helpful in further spectroscopic studies of related compounds.

5 Conclusions

In this work, we have performed a comprehensive characterization of the Raman spectrum of solid-state benzylic amide [2]catenane by means of μ-Raman experiments and first-principles calculations. Despite the complexity of this compound, the agreement found between experimental spectra and calculations is excellent, which allows us to carry out the complete assignment of the main vibrational modes responsible for the Raman spectrum. Additionally, a detailed geometrical description of these modes in terms of the usual normal coordinates is provided. Furthermore, these findings about the molecular structure of this compound could be of great interest in further studies involving the interaction of other mechanically interlocked molecules with their chemical environment or subsequent characterization works using spectroscopic techniques. Finally, the computational approach devised in this work is completely applicable to other systems expecting results with a similar accuracy.

Acknowledgement

We thank Prof. Rubén Pérez and Dr. Pablo Pou for useful discussions.

Supporting Information Available

A set of files (.xyz) with the coordinates of the normal modes collected in Table 1 is provided. Thus, animated visualizations of each mode are possible using standard softwares like Jmol, Avogadro, etc. In addition, a complete study of the normal modes of the benzamide molecule and supplementary figures of the Raman spectra are available in the Supporting Information.

References

1. Schill, G. *Catenanes, Rotaxanes and Knots*; Academic Press, 1971.

2. Amabilino, D. B.; Stoddart, J. F. Interlocked and Intertwined Structures and Superstructures. *Chem. Rev.* **1995**, *95*, 2725–2828.

3. Raymo, F. M.; Stoddart, J. F. Interlocked Macromolecules. *Chem. Rev.* **1999**, *99*, 1643–1664.

4. Kay, E. R.; Leigh, D. A.; Zerbetto, F. Synthetic Molecular Motors and Mechanical Machines. *Angew. Chem. Int. Ed.* **2007**, *46*, 72–191.

5. Erbas-Cakmak, S.; Leigh, D. A.; McTernan, C. T.; Nussbaumer, A. L. Artificial Molecular Machines. *Chem. Rev.* **2015**, *115*, 10081–10206.

6. Leigh, D. A.; Murphy, A.; Smart, J. P.; Deleuze, M. S.; Zerbetto, F. Controlling the Frequency of Macrocyclic Ring Rotation in Benzylic Amide [2]Catenanes. *J. Am. Chem. Soc.* **1998**, *120*, 6458.

7. Leigh, D. A.; Wong, J. K. Y.; Dehez, F.; Zerbetto, F. Unidirectional Rotation in a Mechanically Interlocked Molecular Rotor. *Nature* **2003**, *424*, 174.

8. Johnston, A. G.; Leigh, D. A.; Pritchard, R. J.; Deegan, M. D. Facile Synthesis and Solid-State Structure of a Benzylic Amide [2]Catenane. *Angew. Chem. Int. Ed.* **1995**, *34*, 1209.

9. Johnston, A. G.; Leigh, D. A.; Nezhat, L.; Smart, J. P.; Deegan, M. D. Structurally Diverse and Dynamically Versatile Benzylic Amide [2]Catenanes Assembled Directly from Commercially Available Precursors. *Angew. Chem. Int. Ed.* **1995**, *34*, 1212.

10. Leigh, D. A.; Moody, K.; Smart, J. P.; Watson, K. J.; Slawin, A. M. Z. Catenane Chameleons: Environment-Sensitive Translational Isomerism in Amphiphilic Benzylic Amide [2]Catenanes. *Angew. Chem. Int. Ed.* **1996**, *35*, 306.

11. Fustin, C. A.; Gouttebaron, R.; Nadaï, C. D.; Caudano, R.; Zerbetto, F.; Leigh, D. A.; Rudolf, P. Photoemission Study of Pristine and Potassium Intercalated Benzylic Amide [2]Catenane Films. *Surf. Sci.* **2001**, *474*, 37.

12. Fustin, C. A.; Gouttebaron, R.; Caudano, R.; Rudolf, P.; Leigh, D. A.; Fanti, M.; Krug, A.; Zerbetto, F. Effect of Potassium Intercalation on the Electronic and Vibrational Properties of Benzylic Amide [2]Catenane Films. *Surf. Sci.* **2002**, *515*, 45.

13. Fanti, M.; Fustin, C.-A.; Leigh, D. A.; Murphy, A.; Rudolf, P.; Caudano, R.; Zamboni, R.; Zerbetto, F. High-Frequency Vibrations of the Simplest Benzylic Amide [2]Catenane. *J. Phys. Chem. A* **1998**, *102*, 5782.

14. Fustin, C.-A.; Leigh, D. A.; Rudolf, P.; Timpel, D.; Zerbetto, F. Physical Consequences of a Mechanically Interlocked Architecture: Benzylic Amide Catenane NH Stretching Vibrations as Sensitive Probes for Weakly Hydrogen-Bonding Environments. *ChemPhysChem* **2000**, *1*, 97.

15. Caciuffo, R.; Esposti, A. D.; Deleuze, M. S.; Leigh, D. A.; Murphy, A.; Paci, B.; Parker, S. F.; Zerbetto, F. Inelastic Neutron Scattering of Large Molecular Systems: The Case of the Original Benzylic Amide [2]Catenane. *J. Chem. Phys.* **1998**, *109*, 11094.

16. Deleuze, M. S.; Leigh, D. A.; Zerbetto, F. How Do Benzylic Amide [2]Catenane Rings Rotate? *J. Am. Chem. Soc.* **1999**, *121*, 2364.

17. Deleuze, M. S. Can Benzylic Amide [2]Catenane Rings Rotate on Graphite? *J. Am. Chem. Soc.* **2000**, *122*, 1130.

18. Abuelela, A. M.; Mohamed, T. A.; Prezhdo, O. V. DFT Simulation and Vibrational Analysis of the IR and Raman Spectra of a CdSe Quantum Dot Capped by Methylamine and Trimethylphosphine Oxide Ligands. *J. Phys. Chem. C* **2012**, *116*, 14674–14681.

19. Whale, T. F.; Clark, S. J.; Finney, J. L.; Salzmann, C. G. DFT-Assisted Interpretation of the Raman Spectra of Hydrogen-Ordered Ice XV. *J. Raman Spectr.* **2012**, *44*, 290–298.

20. Liang, L.; Meunier, V. First-Principles Raman Spectra of MoS_2, WS_2 and their Heterostructures. *Nanoscale* **2014**, *6*, 5394–5401.

21. Malik, M.; Wysokiński, R.; Zierkiewicz, W.; Helios, K.; Michalska, D. Raman and Infrared Spectroscopy, DFT Calculations, and Vibrational Assignment of the Anticancer Agent Picoplatin: Performance of Long-Range Corrected/Hybrid Functionals for a Platinum(II) Complex. *J. Phys. Chem. A* **2014**, *118*, 6922–6934.

22. Feng, D.; Zhang, B.; Zheng, G.; Wan, S.; You, J. Raman Spectral and Density Functional Theory Analyses of the CsB_3O_5 Melt Structure. *Inorg. Chem.* **2016**, *55*, 7098–7102.

23. McCreery Group Summary: http://www.chem.ualberta.ca/~mccreery/raman.html (last accessed April 2018).

24. Kresse, G.; Furthmüller, J. Efficient Iterative Schemes for Ab Initio Total-Energy Calculations Using a Plane-Wave Basis Set. *Phys. Rev. B* **1996**, *54*, 11169.

25. Blöchl, P. E. Projector Augmented-Wave Method. *Phys. Rev. B* **1994**, *50*, 17953.

26. Kresse, G.; Joubert, D. From Ultrasoft Pseudopotentials to the Projector Augmented-Wave Method. *Phys. Rev. B* **1999**, *59*, 1758.

27. Perdew, J. P.; Burke, K.; Ernzerhof, M. Generalized Gradient Approximation Made Simple. *Phys. Rev. Lett.* **1996**, *77*, 3865.

28. Grimme, S.; Antony, J.; Ehrlich, S.; Krieg, H. A Consistent and Accurate Ab Initio Parametrization of Density Functional Dispersion Correction (DFT-D) for the 94 Elements H-Pu. *J. Chem. Phys.* **2010**, *132*, 154104.

29. Monkhorst, H. J.; Pack, J. D. Special Points for Brillouin-Zone Integrations. *Phys. Rev. B* **1976**, *13*, 5188.

30. Crystallographic data available at: https://dx.doi.org/10.5517/cc5d0k3.

31. Wilson Jr., E. B.; Decius, J. D.; Cross, P. C. *Molecular Vibrations*; McGraw-Hill, 1955.

32. Woodward, L. A. *Introduction to the Theory of Molecular Vibrations and Vibrational Spectroscopy*; Oxford University Press, 1972.

33. Pei, K.-M.; Ma, Y.; Zheng, X. Resonance Raman and Theoretical Investigation of the Photodissociation Dynamics of Benzamide in S3 State. *J. Chem. Phys.* **2008**, *128*, 224310.

34. Porezag, D.; Pederson, M. R. Infrared Intensities and Raman-Scattering Activities within Density-Functional Theory. *Phys. Rev. B* **1996**, *54*, 7830.

35. Long, D. A. *The Raman Effect: A Unified Treatment of the Theory of Raman Scattering by Molecules*; John Wiley & Sons, 2002.

36. Baroni, S.; Resta, R. Ab Initio Calculation of the Macroscopic Dielectric Constant in Silicon. *Phys. Rev. B* **1986**, *33*, 7017.

37. Gajdoš, M.; Hummer, K.; Kresse, G.; Furthmüller, J.; Bechstedt, F. Linear Optical Properties in the Projector-Augmented Wave Methodology. *Phys. Rev. B* **2006**, *73*, 045112.

Peaks (cm^{-1})		Mode	ν_n	Description
(exp.)	(calc.)	(No.)	(cm^{-1})	
636	641	1146	638	a-in-plane-rd + r-νCH
649		1126	666	s-out-of-plane-rd + πCNCC
808	815	986	815	s-in-plane-rd + δNCC + s-r-νCH
874	874	921	874	s-in-plane-rd + πCNCC + δHCH
999	1001	792	1000	s-in-plane-rd + s-r-νCH
		789	1001	s-in-plane-rd + s-r-νCH
		788	1004	s-in-plane-rd + s-r-νCH
		786	1004	s-in-plane-rd + s-r-νCH
		785	1004	s-in-plane-rd + s-r-νCH
1044	1033	756	1044	δCNC + νCN + s-in-plane-rd
1202	1213	622	1208	s-in-plane-rd + δCCN
		619	1211	s-in-plane-rd + δCCN
1282	1306	570	1267	δCCN + a-in-plane-rd
		558	1287	δCCN + a-in-plane-rd
1301		549	1294	δCCN + a-in-plane-rd
		537	1305	δCCN + a-in-plane-rd
		532	1306	δCCN + a-in-plane-rd
		521	1311	δCCN + a-in-plane-rd
1322		519	1317	τCCNC
1362	1349	491	1348	δCCNC
		481	1354	ωCH2 + δCCN + a-in-plane-rd
1530	1531	340	1523	νCN + δCCN
		333	1529	νCN + νCC
		328	1533	νCN + νCC

Table 1 (Continued on next page)

Continued from previous page

Peaks (cm^{-1})		Mode	ν_n	Description
(exp.)	(theory)	(No.)	(cm^{-1})	
1582		303	1575	νCC + s-in-plane-rd + νCO
		301	1575	νCC + δCCN + in-plane-rd
1599	1597	286	1592	νCC + νCO + δCNC + a-in-plane-rd
		285	1592	νCO + νCC + δCCN + a-in-plane-rd
		276	1597	νCC + νCO + δCNC + a-in-plane-rd
		261	1610	νCC + νCN + δCCN + s-in-plane-rd
		260	1611	νCO + νCN + νCC + δCCN + s-in-plane-rd
1628		243	1620	νCO + νCC + νCN+ δCCN + s-in-plane-rd
		236	1625	νCO + νCN + δCCN + a-in-plane-rd
		232	1634	νCO + νCN + δCNC + a-in-plane-rd
2878	2968	220	2965	s-νCH2
		219	2966	s-νCH2 + δCCN
		218	2968	s-νCH2 + δCCN + νCC + νCN
		217	2968	s-νCH_2 + δCCN + νCC + νCN
		213	2970	s-νCH_2 + δCCN + νCC + νCN
2927		202	2995	s-νCH_2 + δCCN + νCC + νCN
2948	3007	134	3105	a-r-νCH + a-in-plane-rd
		117	3114	s-r-νCH
		115	3115	s-r-νCH
		110	3118	r-νCH + in-plane-rd
3009		79	3138	s-r-νCH + in-plane-rd
		75	3138	s-r-νCH + in-plane-rd
		73	3139	r-νCH + in-plane-rd
3033	3140	63	3146	s-r-νCH + in-plane-rd
		54	3147	r-νCH + in-plane-rd
		50	3147	r-νCH + in-plane-rd
		42	3151	r-νCH + in-plane-rd
		38	3170	r-νCH + in-plane-rd

Table 1 (Continued on next page)

Continued from previous page

Peaks (cm^{-1})		Mode	ν_n	Description
(exp.)	(theory)	(No.)	(cm^{-1})	
3291	3310	32	3309	νNH + νCN + δCNC
		31	3309	νNH + νCN + δCNC
3322	3340	20	3340	νNH + νCN
3362	3410	8	3410	νNH
		5	3410	νNH + νCN

Table 1: Comparison between the main peaks of the experimental Raman spectrum and those of the theoretical calculation. The assignment of the selected normal modes are given in terms of usual internal coordinates of vibration. They are ordered by decreasing contribution to the corresponding normal mode. Internal coordinates: ν, stretching; δ, in-plane bending; π, out-of-plane bending; τ, torsion and ω wagging. Additional labels: a, antisymmetric; r, benzene ring; rd, benzene ring deformation; s, symmetric.

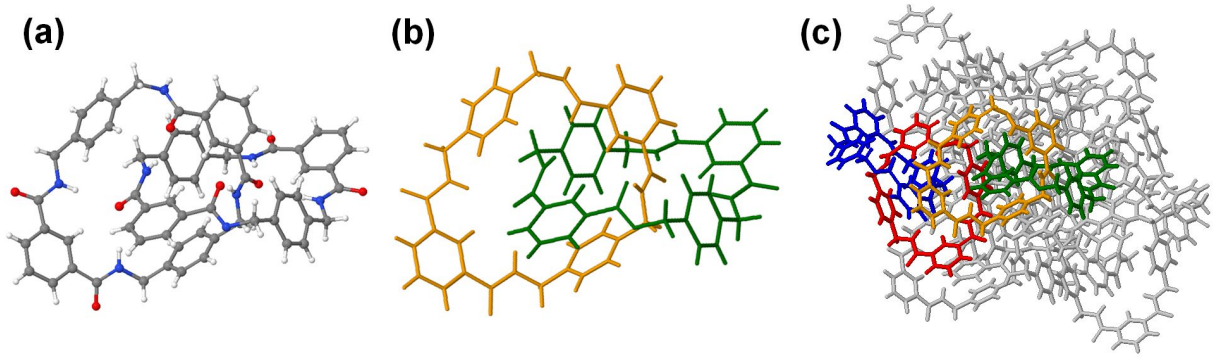

Figure 1: Molecular and crystal structure of the benzylic amide [2]catenane: Molecular structure as embedded in the crystal structure, ball-and-stick model (a) and two-color simplified model showing the two different macrocycles (b). Crystal packing of the molecules in the crystalline state (c). Some macrocyclic units are highlighted in colors to ease the visualization.

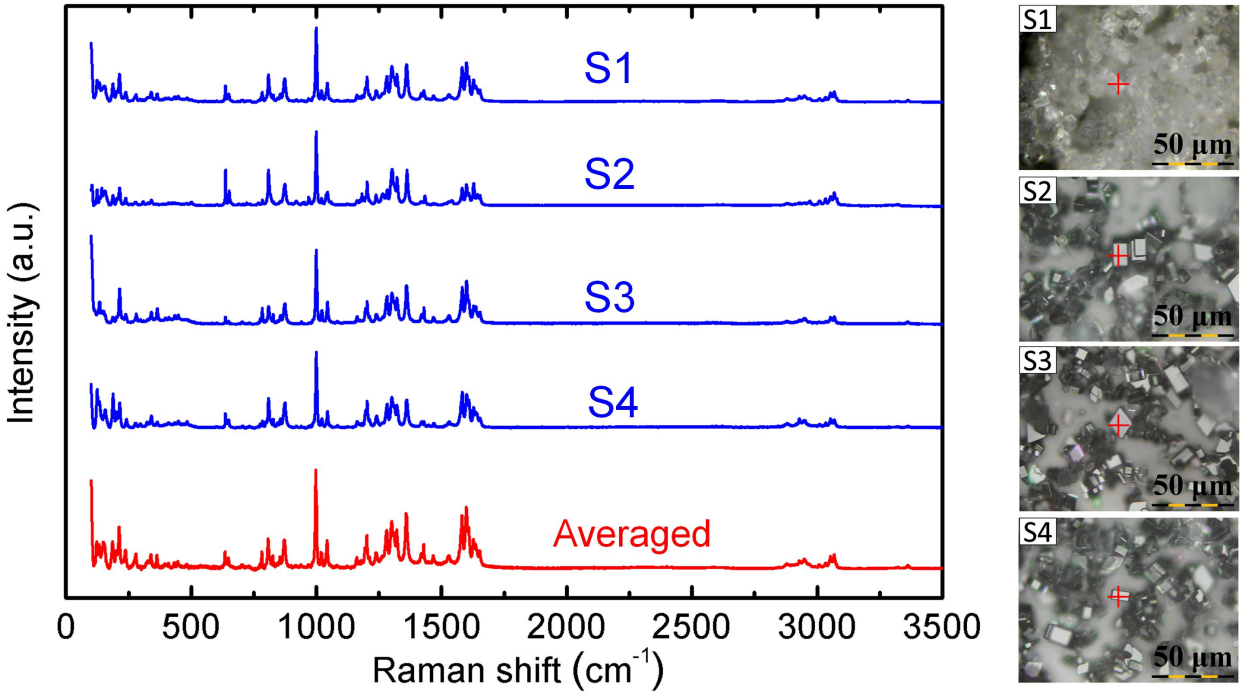

Figure 2: Raman spectra (S1-S4 and averaged) of several crystals of benzylic amide [2]catenane with different shapes, according to the microphotographs shown in the right panel. These microphotographs were made with an LWD eyepiece (50×) and the exact location where the spectra were recorded are depicted with a red cross.

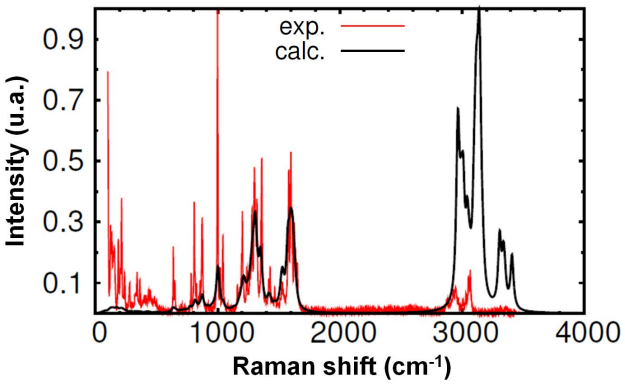

Figure 3: Comparison between the calculated Raman spectrum (black line) and the experimental averaged spectrum (red line) obtained by μ-Raman.

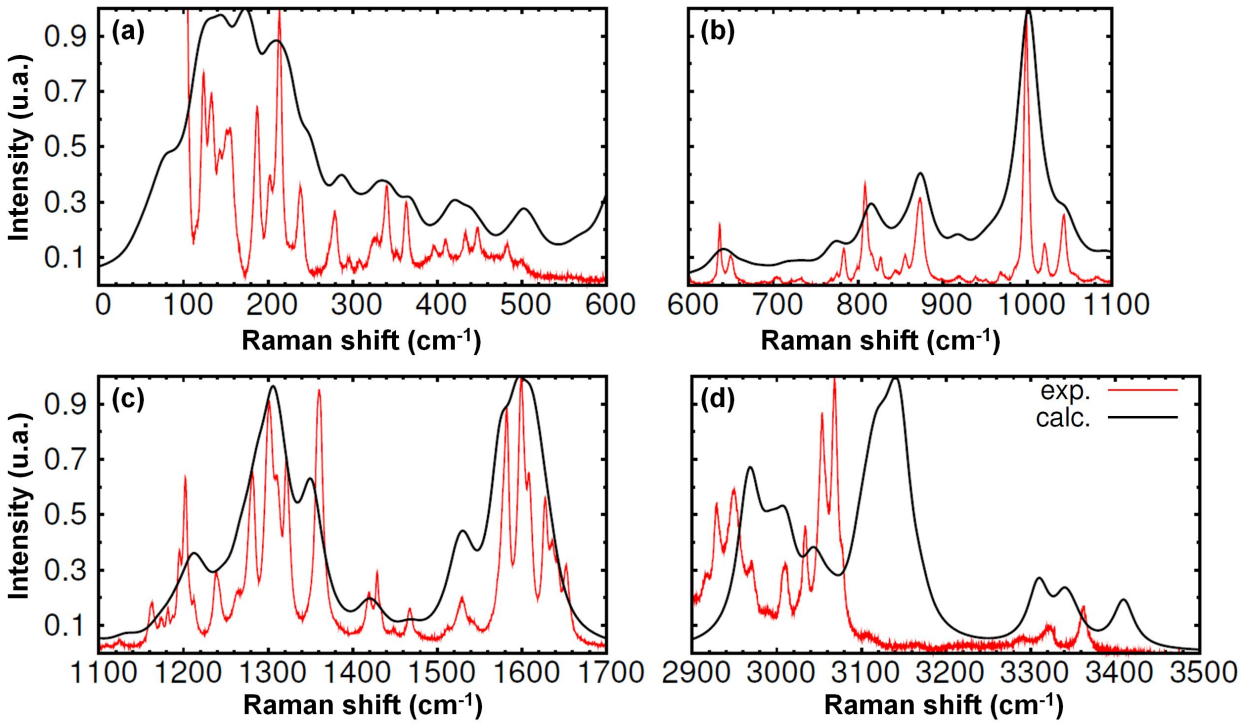

Figure 4: Comparison between the calculated Raman spectrum (black line) and the experimental averaged spectrum (red line) after renormalization in different wavenumber regions. See text for further details.

Graphical TOC Entry